Biosensors and Bioelectronics 126 (2019) 108–114

Contents lists available at ScienceDirect

Biosensors and Bioelectronics

journal homepage: www.elsevier.com/locate/bios

Label-free electrochemical immunosensor for insulin detection by high-efficiency synergy strategy of Pd NPs@3D MoS_x towards H_2O_2

Zengqiang Gao[a,b], Yueyun Li[a,*], Chunyan Zhang[a], Shuan Zhang[a], Faying Li[b,c], Ping Wang[a], Huan Wang[b,*], Qin Wei[b]

[a] School of Chemistry and Chemical Engineering, Shandong University of Technology, Zibo 255049, PR China
[b] Key Laboratory of Interfacial Reaction & Sensing Analysis in Universities of Shandong, School of Chemistry and Chemical Engineering, University of Jinan, Jinan 250022, PR China
[c] Institut National de la Recherche Scientifique, Centre for Energy, Materials, and Telecommunications, 1650 Boulevard Lionel-Boulet, Varennes, Québec, Canada J3X 1S2

ARTICLE INFO

Keywords:
Electrochemical label-free immunosensor
Amorphous MoS_x
Insulin
Pd NPs
CTAB

ABSTRACT

Here, a novel H_2O_2-based electrochemical immunosensor utilizing Pd nanoparticles functionalized three-dimensional wrinkly amorphous MoS_x composites (Pd NPs@3D MoS_x) as the platform was developed for the determination of insulin. In this work, Pd NPs@3D MoS_x prepared in the presence of CTAB possessed an excellent catalytic activity for the reduction of H_2O_2. Furthermore, Pd NPs@3D MoS_x with favorable biological compatibility can conjugate a great many antibodies to capture insulin. Attributed to the excellent property, electrochemical signals could be greatly amplified, contributing to improving detection sensitivity. Especially, SEM, TEM, and XPS information further confirmed nanomaterial's surface morphology and amorphous structure. Under the optimal conditions, the proposed immunosensor exhibited a sensitively linear relation with logarithmic insulin concentrations from 0.01 to 100 ng/mL with a low detection limit of 3.0 pg/mL (S/N = 3). Characterized by good reproducibility, specificity, and stability, the fabricated immunosensor may blaze a path for insulin detection in a real sample.

1. Introduction

Insulin, a peptide hormone produced by pancreatic islet beta cells, is regarded as the key anabolic hormone in vivo (Hsieh et al., 2006). It not only promotes absorption of glucose from the blood into adipocytes, liver and skeletal muscle cells but also regulates the metabolism of carbohydrates, fat, and protein. For example, a high concentration of insulin in the blood strongly inhibits the production and secretion of hepatic glucose (Zhu et al., 2017). Meanwhile, circulating insulin can influence proteins synthesis in widely various tissues (Saltiel and Kahn, 2001). More importantly, insulin can also affect vascular cognition and compliance. Once insulin diffused to the human brain, learning and memory can be promoted, especially for verbal memory (Benedict et al., 2004). If insulin dysfunctions, it will trigger diabetes mellitus and heighten the risk of kidney failure, myocardial infarction, obesity, and neurodegenerative disease in patients with diabetes and hyperinsulinemia (Schutte et al., 2015; Wang et al., 2018). Hydrogen peroxide (H_2O_2) is not only of great significance in the fields of bioanalysis as well as clinical, pharmaceutical, and environmental applications but also playing a momentous role in regulating various biological processes, including vascular remodeling, immune cell activation, and apoptosis, as a byproduct of large-scale biological processes (Wang et al., 2013). Therefore, it is significant to propose a highly sensitive and specific strategy for highly electrocatalytic activity toward the reduction of H_2O_2 to achieve the diagnosis of insulin in clinical analysis.

As the rapid development of analytical technique, more and more methods have been used to diagnose the insulin, such as high performance liquid chromatography (HPLC) (Mercolini et al., 2008), enzyme-link immunosorbent assays (ELISA) (Heyduk et al., 2010), flow injection analysis (Salimi et al., 2009), turbidimetry (Jasuja et al., 2012), and so forth. Nonetheless, some of the analytical strategies have been too cumbersome, time-consuming, and expensive, hindering the universal detection of insulin. Therefore, the electrochemical immunosensor, based on the highly antigen-antibody specific interaction, has attracted extensive attention, due to its advantage of high sensitivity and specificity, fast response, ease of operation, easy miniaturization, and simple instrumentation (Han et al., 2016; Jiang et al., 2015; Li et al., 2015).

To detect biomarkers, immunosensors demand a highly conductive and catalytic substrate by an easily constructed protocol. Recently,

* Corresponding authors.
E-mail addresses: liyueyun@stdut.com (Y. Li), wanghuan8711@163.com (H. Wang).

https://doi.org/10.1016/j.bios.2018.10.017
Received 4 July 2018; Received in revised form 27 September 2018; Accepted 8 October 2018
Available online 13 October 2018
0956-5663/

considerable attention has been drawn to Molybdenum disulfide (MoS_2) as the typical representatives of transition metal dichalcogenides in the field of nanoelectronics (Radisavljevic and Kis, 2013), because of its fantastic electronic and physical properties and promising applications in electrocatalysis, photocatalysis, supercapacitors, lithium-ion batteries, and chemical sensors (Maitra et al., 2013; Wang et al., 2013). The previous study demonstrated that the basal plane of MoS_2 was catalytically inert. Whereas, there was covered with catalytically active sites in the edge plane with high surface energy (Tan et al., 2015). Thanks to highly electrocatalytic activity and binding energy with atomic hydrogen, MoS_2 was considered as a potential ideal replacement for platinum group catalysts (Karunadasa et al., 2012). Furthermore, many researchers reported that MoS_2 could effectively combine with other nanomaterials to achieve excellent catalytic activity (F. Li et al., 2018; Xu et al., 2015). And, amorphous molybdenum sulfide (MoS_x) with an optimized structure and morphology exposed more active edge sites for electrocatalytic activity (Ting et al., 2016). In addition, the intrinsically abundant defect sites in MoS_x were presented throughout the entire surface of the catalyst and readily available for catalytic reactions (Laursen et al., 2013; F. Li et al., 2018). As is known, MoS_x by a cost-effective method have been widely applied to oxygen reduction reaction (ORR) (Ahmed and Gerischer, 1979) and hydrogen evolution reaction (HER) (Hinnemann et al., 2005). Meanwhile, surfactants aroused researchers' particular interest in electrochemistry, owing to surface active and amphiphilic molecules (Wu et al., 2006). More importantly, the participation of polar surfactant in the solution may improve the aqueous solubility of nanomaterials, resulting in significant change in redox properties and electroanalytical properties (Rather and De Wael, 2012). Among these positive strategies, cetyltrimethylammonium bromide (CTAB) as a cationic surfactant played a crucial role in adjusting the surface structures of nanomaterial and ensuring effective and stable dispersion, such as promoting the electron transfer process. As has been reported, noble metal nanoparticles, especially palladium nanoparticles (Pd NPs), have sparked extensive concerns thanks to superior biocompatibility (Wang et al., 2014). The Pd NPs could effectively improve the conductivity of amorphous MoS_x, couple a great many antibodies by Pd-N bond, and enhance the catalytic activity to enlarge the detection signal (Liu et al., 2016).

A label-free immunosensor was fabricated in this work for insulin detection. Three-dimensional wrinkly amorphous MoS_x (3D MoS_x), with the high accessible surface area and more active probes and domains, was modified by CTAB. Furthermore, a simple method was applied to synthesize Pd NPs functionalized 3D wrinkly amorphous MoS_x (Pd NPs@3D MoS_x). Crucially, the Pd NPs integrated on 3D MoS_x can not only provide a suitable platform for immobilizing the biomolecules via the Pd-N bond but also further promote the catalytic properties of the catalyst towards the reduction of H_2O_2 by synergetic effects. Remarkably, 3D MoS_x, as the less expensive nanomaterial, efficaciously reduced the consumption of Pd-group material and achieved an excellent performance in signal amplification.

2. Experimental section

2.1. Materials

Insulin antigen and antibody were obtained from Shanghai Linc-Bio Science Co. Ltd. (Shanghai, China). Polyvinylpyrrolidone (PVP, K30), ammonium molybdate tetrahydrate ($(NH_4)_6Mo_7O_{24}{\cdot}4H_2O$), and bovine serum albumin (BSA, 96–99%) were purchased from Sigma-Aldrich (Beijing, China). Palladium (II) chloride ($PdCl_2$, A.R.), thiourea (NH_2CSNH_2), cetyltrimethylammonium bromide (CTAB), and ascorbic acid (AA) were obtained from Macklin Biochemical Co., Ltd. (Shanghai, China). The level of involved reagents was of analytical grade and used without further purification. Deionized water (18.25 MΩ cm) was used in all the experimental processes.

2.2. Apparatus

Scanning electron microscopy (SEM) was performed by the FEI QUANTA FEG250 coupled to an INCA Energy X-MAX-50. TEM and HRTEM images were characterized by The JEOL MODEL JEM-2100F transmission electron microscope (TEM). X-ray photoelectron spectroscopy (XPS) measurements were performed by ESCALAB 250 XI with a monochromatic Al Kα source. And X-ray diffraction (XRD) patterns were completed by the D8 focus diffractometer. The electrochemical measurements were performed on CHI760E workstation (Chenhua Instrument Shanghai Co., Ltd, China) using a three-electrode system including a glassy carbon electrode (GCE, Φ = 4 mm) as the working electrode, a platinum wire as the counter electrode, and a saturated calomel electrode (SCE) as the reference electrode.

2.3. Preparation of 3D MoS_x

Typically, 14 mmol NH_2CSNH_2, 1 mmol $(NH_4)_6Mo_7O_{24}{\cdot}4H_2O$, and surfactant PVP were dissolved gradually in 35 mL deionized water under sonication. Following that, the solution was heated at 220 °C for 18 h. After cooling to room temperature, the obtained precipitate was centrifuged and washed with water several times. The final product was freeze-dried. For the synthesis of 3D radially oriented MoS_2 nanospheres (3DR-MoS_2), the protocol was essentially carried out according to the former report (Zhang et al., 2015). The defect-rich MoS_2 ultrathin nanosheets (defect-rich MoS_2) was synthesized according to the previous literature (Xie et al., 2013).

2.4. Preparation of Pd NPs@3D MoS_x

In a typical reaction, 2 mg 3D MoS_x was dissolved into an aqueous solution (8 mL) containing 0.05 mM CTAB under sonication for 20 min, and then the solution was centrifuged at 8000 rpm for 5 min and subsequently dispersed in 10 mL to minimize residual surfactants. After that, 20 mL 1 mM H_2PdCl_4 aqueous solution was injected into the suspension under ultra-sonication for another 10 min. Followed by the rapid injection of 1 mL of 1 mmol/mL AA aqueous solution as reductant, the suspension continuously was shaken for several minutes, and then left undisturbed for at least 6 h. Finally, the black-brown precipitate was obtained by consecutive washing cycles for several times with ethanol and water twice and then was freeze-dried.

2.5. Preparation of electrochemical immunosensor

The fabrication process of the immunosensor was illustrated in Fig. 1. The bare GCE was polished by alumina slurries to a mirror and sequentially washed with deionized water. Following that, the GCE was modified with 6 μL of the Pd NPs@3D MoS_x solution and dried at room temperature. Following that, 6 μL of antibody (10 μg/mL) was incubated on the GCE overnight at 4 °C. After washing the modified electrode with the PBS (pH 7.4), 3 μL of BSA (1%) was dropped on the modified GCE to block the nonspecific binding sites and washed thoroughly with the PBS (pH 7.4). At last, the fabricated electrode was stored at 4 °C for further research.

2.6. Insulin detection

Above all, the fabricated immunosensor was incubated with insulin for 1 h and then washed with PBS to remove the unbounded insulin. Subsequently, the electrochemical measurements were carried out by amperometric *i-t* measurement. The potential of −0.4 V was chosen as scanning potential so as to reduce the background current and minimize the common interference responses. After the baseline was stabilizing, 10 μL 5.0 mol/mL H_2O_2 was injected into the PBS (10 mL) under moderately stirring and then the current was recorded by the amperometric i-t current curve.

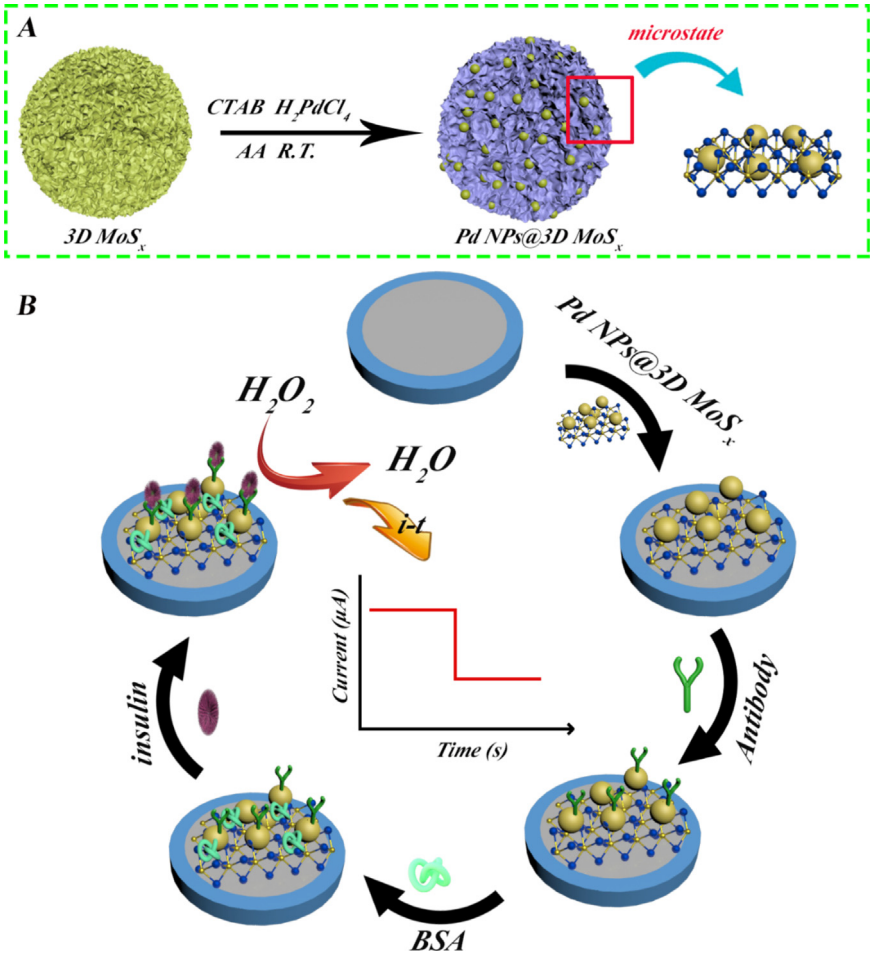

Fig. 1. Illustration of the fabricated immunosensor for insulin detection (B), the fabrication of Pd NPs@3D MoS_x (B).

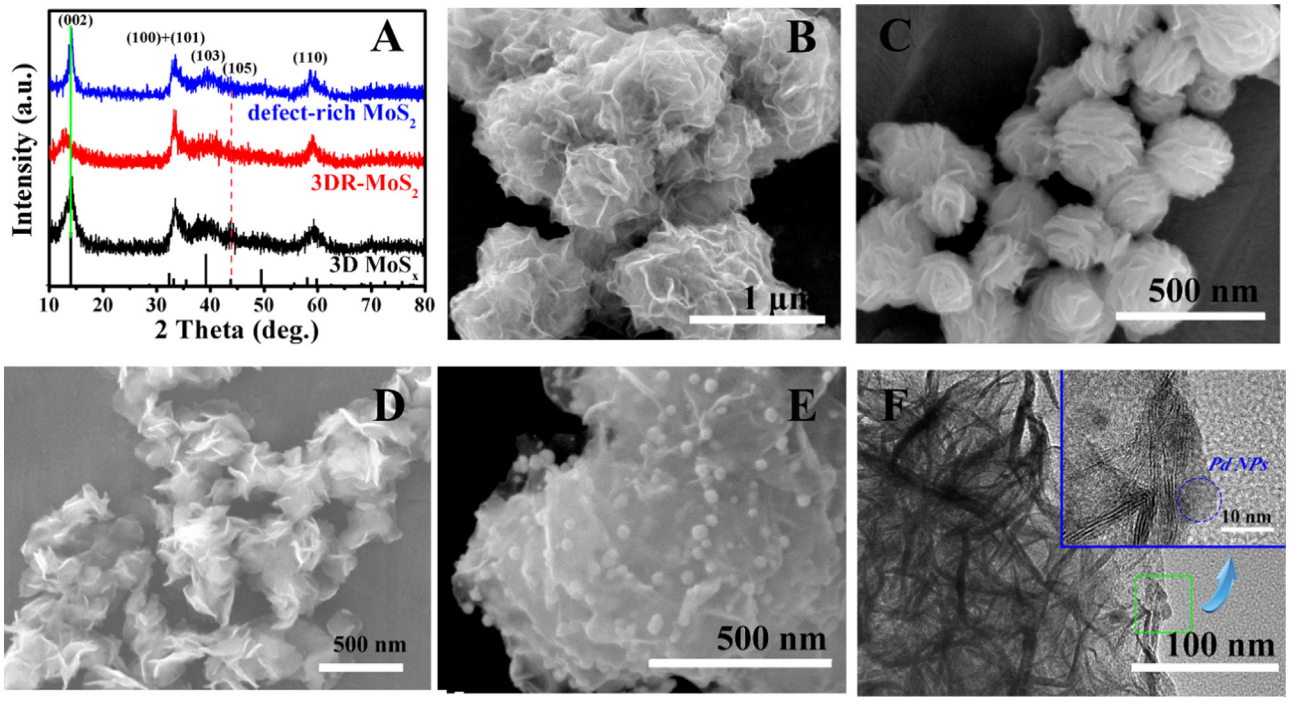

Fig. 2. The XRD pattern of different materials (A); SEM image of: 3D MoS_x (B), 3DR-MoS_2 (C), defect-rich MoS_2 (D), and Pd NPs@3D MoS_x (E); TEM imagine of Pd NPs@3D MoS_x (inset, HETEM) (F).

3. Results and discussion

3.1. Material characterization

Fig. 2B illustrated the SEM image of the 3D MoS_x. Obviously, the as-prepared MoS_x exhibited a sphere-like structure with the rough surface, continuous ripples, and abundant crumpled edge. The 3DR-MoS_2 (shown in Fig. 2C) exhibited large thickness, compared to the 3D MoS_x. Fig. 2D clearly revealed the irregular nanosheet morphology with approximately 200 nm in lateral size. To further explore the crystallographic structures of amorphous MoS_x, the different samples were characterized by X-ray diffraction (XRD). As demonstrated in Fig. 2A, all of the identified peaks can be indexed precisely to the standard pattern of hexagonal MoS_2 (JCPDS card No.37–1492). Significantly, compared to the bulk MoS_2 powder (shown in Fig. S1), the 2θ of diffraction peak (002) for 3D MoS_x, 3DR-MoS_2, and defect-rich MoS_2 was transferred from the standard angle (14.378°) to the lower angle of 14.038°, 12.48°, and 14.084°, revealing larger interlayer distance of 6.3 Å, 7.1 Å and 6.3 Å, respectively. Meanwhile, 3D MoS_x presented broader peaks in intensity and better crystal structure. The results were also proved that involvement of PVP had little influence in the structure of 3D MoS_x.

Notably, the disordered atomic arrangement attributed to the formation of additional edges. From SEM in Fig. 2E, the Pd NPs was uniformly distributed in 3D MoS_x, with the average size of 20 nm. The TEM image in Fig. 2F suggested the orientations of individual (002) planes in 3D MoS_x were highly multifarious, and apparent corrugation can be observed. Besides, the thickness was composed of less than five S-Mo-S layers (inset of Fig. 2F), verifying the preservation of the ultrathin nanosheet structure. Remarkably, the correspondingly disordered basal-surface atomic arrangement generated considerably additional active edge sites. Furthermore, the HRTEM image of the nanoparticle with a lattice spacing of 0.236 nm, which attributed to the (111) lattice of Pd NPs. And high-angle annular dark-field scanning TEM (shown in Fig. S2) was also performed to investigate the spatial distribution of different elements. The highly homogeneous distribution of Pd elements was clearly visualized in energy-dispersive X-ray mapping of the selected regions, confirming Pd NPs was successfully incorporated into the MoS_x structure. And the atomic S/Mo ratio was approximately 3:1, indicating sulfur atoms were unsaturated.

The chemical state and composition of 3D MoS_x were confirmed by XPS measurement. To reduce the charge effect of the samples, the binding energy was calibrated by reference to the C 1s peak (284.6 eV). The XPS survey spectrum in Fig. 3A indicated the presence of Mo, C, O and S elements. The atomic S/Mo ratio was approximately 3:1, indicating sulfur atoms were unsaturated. And the S 2p spectrum in Fig. 3B further verified the existence of the unsaturated sulfur atoms (S_2^{2-}). The S 2p doublet at 161.6 eV can be considered as the bridged S_2^{2-} or apical S^{2-}. The S 2p doublet at 162.7 eV can be considered as the basal plane S^{2-} or terminal S_2^{2-} (Dubouis et al., 2018).

Fig. 3C displayed detailed XPS scans for the binding energy of Mo element. The binding energies of 228.4 and 231.5 eV were respectively attributed to Mo $3d_{5/2}$ and Mo $3d_{3/2}$, which can be relevant to Mo^{IV} and Mo^{V} (Chang et al., 2013). The peak at 225.9 eV can be indexed as S 2s. The peak at 235.3 eV was associated with Mo^{VI}, suggesting that the sample may contain a set number of amorphous MoS_3 (Benck et al., 2012). There are two strong peaks at 232.1 eV and 228.9 eV, which can be ascribed to MoS_2 and MoS_3, respectively (Merki et al., 2011).

3.2. Electrocatalytic activity towards H_2O_2 reduction

The performance of electrodes modified with different composite was investigated through amperometric *i-t* methods. As illustrated in Fig. S3A, the current response of different electrodes followed the order: 3D MoS_x /GCE > defect-rich MoS_2/GCE > bulk MoS_2 sheets/GCE > 3DR-MoS_2/GCE. That might be ascribed to the large surface area, continuous ripples, and abundant wrinkled active edge of 3D MoS_x.

In order to investigate the effect of CTAB, the amperometric *i-t* test was further carried out. As shown in Fig. S3B, there was a larger current response appeared in the presence of CTAB, compared to the absence of CTAB. For the dispersion obtained in the presence of CTAB, it imparted positive charge to absorb anions, due to -$N(CH_3)_3$ and -$(CH_2)_{12}$ protons of CTAB (Gupta et al., 2015), when there was absence of CTAB, it is negative (Pandit et al., 2016). Therefore, more $PdCl_4^{2-}$ ions can be well absorbed on amorphous MoS_x by interparticle electrostatic attraction, and subsequently reduced uniformly on amorphous MoS_x composites by weak reductant AA at room temperature. Thus, CTAB can not only ensure effective and stable dispersion but also promote tremendously the synergetic effects of amorphous MoS_x composites and Pd NPs.

3.3. Mechanism of hydrogen peroxide decomposition on Pd NPs

The new study revealed that the decomposition of hydrogen peroxide on Pd NPs occurred via the peroxide-oxide mechanism (Serra-Maia et al., 2018). Firstly, H_2O_2 reacted with the surface of Pd NPs to form Pd (O) state, releasing one molecule of H_2O. Next, anther molecule of H_2O_2 reduced Pd (O) to metallic Pd, producing H_2O and O_2. More Pd (O) incorporated at the surface possessed a faster decomposition rate of H_2O_2 due to skipping the rate-limiting step of the reaction (the first cycle). The catalytic activity was enhanced for larger Pd NPs due to their lower work function, which increased the rate at which surface Pd atoms reacted with H_2O_2 to form Pd(O) (rate-limiting step).

$$Pd + H_2O_2 \rightarrow H_2O + Pd\ (O) \quad (1)$$

$$Pd\ (O) + H_2O_2 \rightarrow Pd + O_2 + H_2O \quad (2)$$

3.4. Characterization of the immunosensor

The EIS was utilized to evaluate the assembly process of the immunosensor (Feng et al., 2018). The Nyquist plots of A.C. impedance were recorded from 1 to 10^5 Hz at 0.22 V in an electrolyte containing 2.5 mM $[Fe(CN)_6]^{3-/4-}$. In the Nyquist plot, semicircle portion reflected the restricted diffusion of the redox probe at the electrode interface, responding to the charge transfer resistance (R_{et}), and the Randles equivalent circuit as shown in the inset. Obviously, R_{et} was suitable to reflect the interfacial properties of the prepared immunosenor (F. Li et al., 2018; M. Li et al. 2018). As illustrated in Fig. 4A, the bare GCE exhibited the R_{et} value was 56.07 Ω. With the successful assembly of Pd NPs@3D MoS_x onto the GCE, the R_{et} value decreased to 32.67 Ω, verifying that Pd NPs@3D MoS_x can effectively accelerate electron transfer rate. After the modified electrode was assembled by the antibody, BSA, and insulin, the resistance increased gradually (79 Ω, 160.9 Ω, and 194 Ω, respectively), due to the formed insulated immunocomplex as the blocking layer hindering the electron diffusion. EIS information confirmed that the immunosensor was successfully developed.

Besides, the influence of scan rate on the redox peak current of Fe^{2+} and Fe^{3+} was evaluated using Pd NPs@3D MoS_x modified GCE at different scan rates. As demonstrated in Fig. 4B, both of anodic and cathodic peak currents became larger with the increase of scan rate. The linear proportion to the peak current of CVs and the square root of the scan rate in Fig. 4C indicated that the electron transfer of Pd NPs@3D MoS_x surface was diffusion-controlled (Yi et al., 2015).

3.5. Optimization of experimental conditions

To achieve an ideal performance of the proposed immunosensor, experimental conditions (with 1 ng/mL insulin) including the concentration of Pd NPs@3D MoS_x and the pH value were evaluated in this experiment. The pH of PBS was firstly investigated in this work. As illustrated in Fig. S4A, the optimal value of the signal response occurred

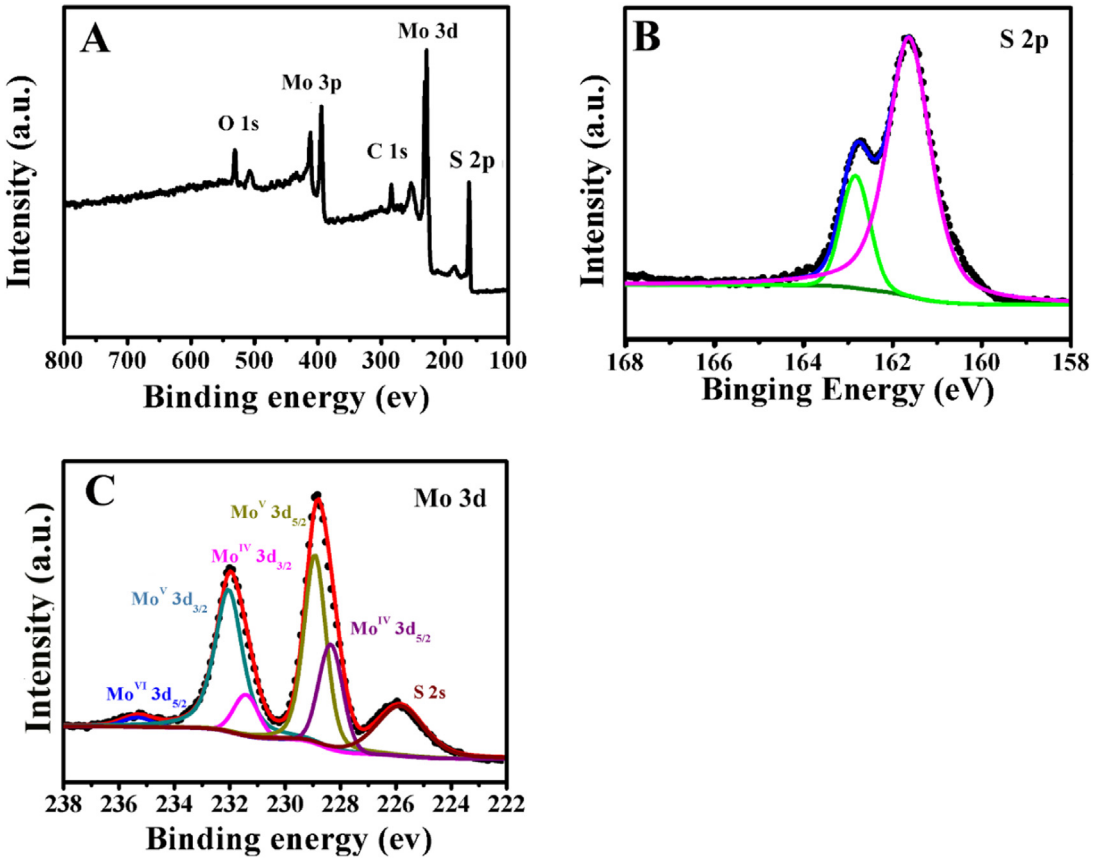

Fig. 3. XPS survey spectrum (A) and XPS high-resolution spectra of S 2p (B) and Mo 3d (C) of 3D MoS_x.

within the range of 5.8–8.0 in 7.4. Furthermore, antibody and antigen could maintain their activity in the neutral environment (Gao et al., 2018; Shi et al., 2017). Thus, pH 7.4 was selected as the optimal pH value. Additionally, the concentration of Pd NPs@3D MoS_x was also studied in this study. As demonstrated in Fig. S4B, the optimal value appeared in 2 mg/mL within the range from 0.5 to 2.5 mg/mL. Thus, 2 mg/mL was chosen as the optimal concentration in this work.

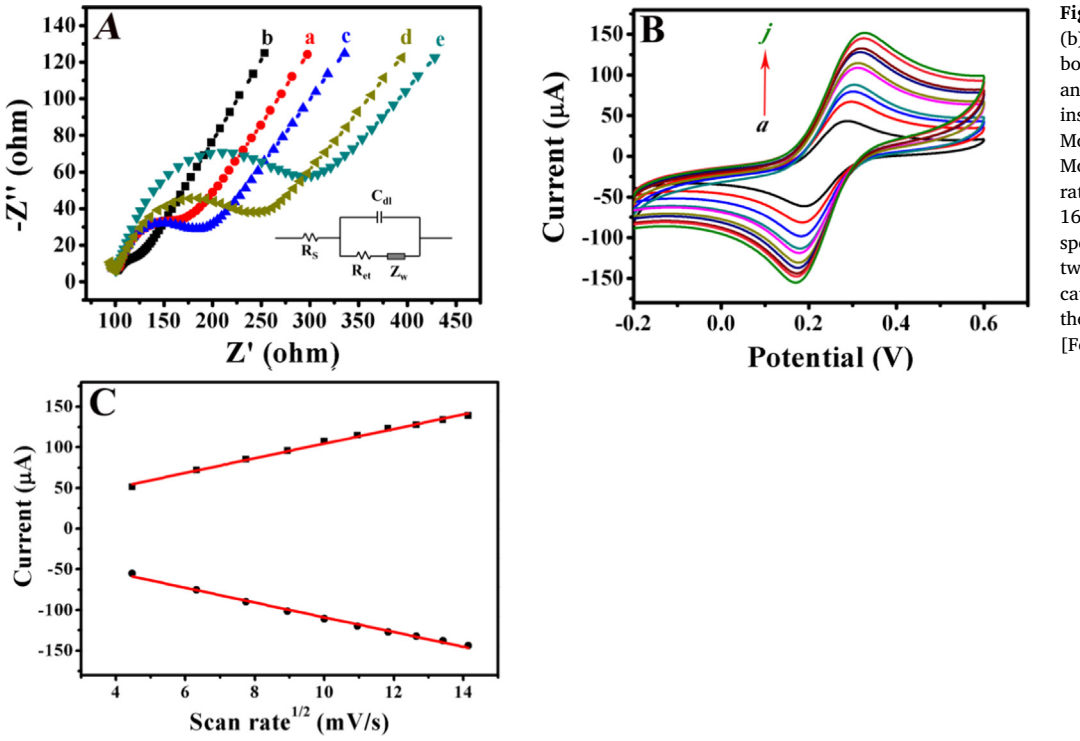

Fig. 4. (A) EIS responses: (a) bare GCE, (b) Pd NPs@3D MoS_x/GCE, (c) antibody/Pd NPs@3D MoS_x/GCE, (d) BSA/antibody/Pd NPs@3D MoS_x/GCE, (e) insulin/BSA/antibody/ Pd NPs@3D MoS_x/GCE; (B) CVs of the Pd NPs@3D MoS_x modified GCE at different scan rates of 20, 40, 60, 80, 100, 120, 140, 160, 180, and 200 mV/s (a→j), respectively. (C) The relationship between the peak currents with the cathodic and anodic peak current and the square root of the scan rate (5 mM $[Fe(CN)_6]^{3-}$).

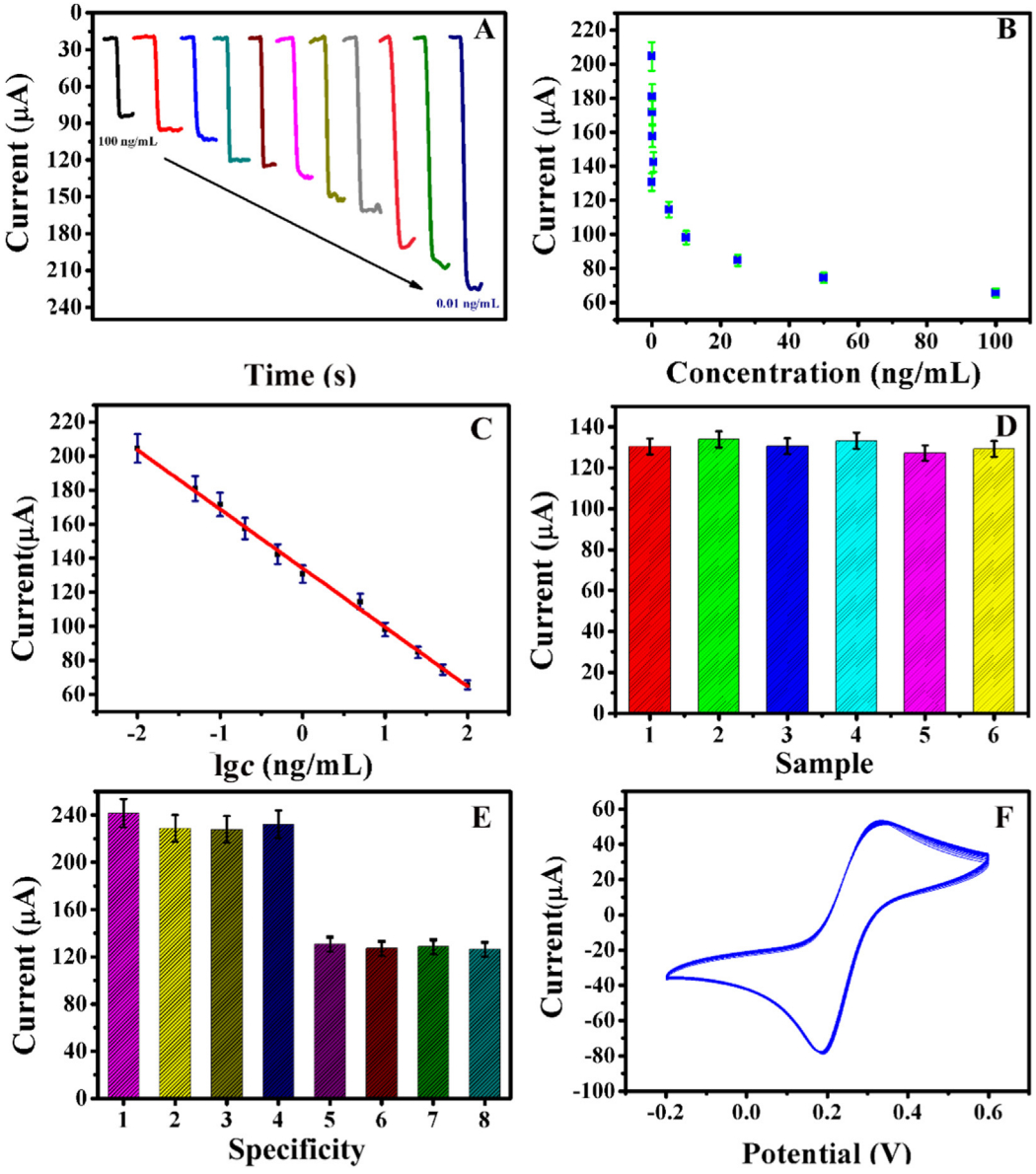

Fig. 5. (A), (B) The signal responses of the proposed immunosensor of different insulin concentration; (C) Calibration curve of the proposed electrochemical immunosensors incubated with a series of concentrations of insulin from 0.01 ng/mL to 100 ng/mL; (D) Reproducibility of the proposed immunosensor with 1 ng/mL insulin; (E) Signal response of the immunosensor to Blank (1), Blank + 50 ng/mL IgG (2), Blank + 50 ng/mL PSA (3), Blank + 50 ng/mL CEA (4), 1 ng/mL insulin (5), 1 ng/mL insulin + 50 ng/mL IgG (6), 1 ng/mL insulin + 50 ng/mL PSA (7), 1 ng/mL insulin + 50 ng/mL CEA (8).; (F) Stability of the proposed immunosensor under successive CV scans for 60 cycles. Error bars = SD (n = 3).

Table 1
Results for the detection of insulin in serum samples.

Initial insulin in the diabetic sample (ng/mL)	Addition content (ng/mL)	The detection content (ng/mL)	RSD (%)	Recovery (%)
1.07	1.00	1.97, 1.89, 1.93, 1.96, 2.11	4.21	95.3
	2.00	3.15, 3.17, 3.21, 3.13, 3.11	1.22	102.8
	5.00	6.13, 5.96, 5.96, 5.86, 5.89	1.76	98.19

3.6. Performance of the developed immunosensor

The developed immunosensors incubated with various concentrations of insulin were investigated based on the optimal conditions. As illustrated in Fig. 5A, the signal response was declining with the increasing concentration of insulin. Nevertheless, as shown in Fig. 5B, the current changed rapidly at the lower concentration of insulin, due to the fast change of steric hindrance. And signal responses tended to flatten out at higher concentration, due to the large steric hindrance and the limited binding sites. Thus, the linear relationship between the logarithmic concentration value of insulin and the current response was illustrated in Fig. 5C. It revealed that the signal response decreased, as the increase in insulin concentration from 0.01 to 100.0 ng/mL. The regression equation was $I = 134.17 - 34.68$ lg$c$ (ng/mL), with a correlation coefficient of 0.997. And the limit of detection was 3.0 pg/mL (S/N = 3). This may attribute to the admirable properties of the 3D

MoS_x, which played the significant part in demonstrating satisfactory detection result with a better linear range and lower limit of detection. Compared to the reported work (Table S1), the proposed immunosensor exhibited a low limit of detection and wide linear range for insulin detection.

3.7. Reproducibility, specificity, and stability of immunosensor

The excellent reproducibility was regarded as one of the most significant factors for evaluating the precision of the prepared immunosensor. In Fig. 5D, six replicative immunosensors for insulin detection (1 ng/mL) were investigated in 10 mL PBS (pH 7.4). The relative standard deviation (RSD) of six repeated measurements with this method was 1.9%, implying that the designed immunosensor displayed a favorable reproducibility.

The specificity of the proposed immunosensor for insulin detection was utilized to demonstrate its feasibility (Feng et al., 2017). Prostate-specific antigen (PSA), immunoglobulin G (IgG) and carcinoembryonic antigen (CEA) were considered as diverse interfering species (50 ng/mL) and mixed with 1 ng/mL of insulin. As illustrated in Fig. 5E, no distinct change of current signal was produced when the interferent was added, and the relevant variation was less than 5%, exhibiting negligible fluctuation. The result further showed that the proposed immunosensor for insulin detection possessed superior specificity.

Furthermore, the stability was an essential analytical parameter to monitor the performance of the proposed immunosensor. As shown in Fig. 5F, successive cyclic voltammetry scans for 60 cycles were carried out after incubated with 5 ng/mL insulin, and the current change was less than 5%, demonstrating an acceptable stability of the proposed immunosensor. Significantly, as shown in Fig. S5, the long-term storage stability of the proposed immunosensor was further investigated after storage at 4 ˚C, and the current still remained 89.7% after 18 days. The results above testified that the proposed immunosensor possessed potential practical value.

3.8. Real sample analysis

For the sake of evaluating the reliability of the immunosensor in the practical application, the human serum was diluted adequately with PBS (neutral) previous to detecting. As illustrated in Table 1, the recovery range from 95.3% to 102.8% and RSD from 1.22% to 4.21% indicated that the designed immunosensor had acceptable sensitivity and accuracy, which suggested immunosensor had promising potential for insulin detection in the biological samples.

4. Conclusion

In short, an effective label-free immunosensor was fabricated for insulin detection based on Pd NPs@3D MoS_x via in-situ reduction at room temperature. Pd NPs could evenly coordinate with 3D MoS_x, which not only provided better conductivity and excellent biocompatibility but also allowed a new perspective for the reduction of H_2O_2. The designed immunoassay could provide repaid signal responses for insulin detection, making it an effective modality for detection. Moreover, this approach probably provided a promising opportunity for real diagnosis.

Acknowledgement

This study was supported by National Natural Science Foundation of China (No. 21575079), the Key Research and Development Program of Shandong Province (No. 2018GSF120001), the National Key Scientific Instrument and Equipment Development Project of China (No. 21627809).

Appendix A. Supporting information

Supplementary data associated with this article can be found in the online version at doi:10.1016/j.bios.2018.10.017.

References

Ahmed, S.M., Gerischer, H., 1979. Electrochim. Acta 24 (6), 705–711.
Benck, J.D., Chen, Z., Kuritzky, L.Y., Forman, A.J., Jaramillo, T.F., 2012. ACS Catal. 2 (9), 1916–1923.
Benedict, C., Hallschmid, M., Hatke, A., Schultes, B., Fehm, H.L., Born, J., Kern, W., 2004. Psychoneuroendocrinology 29 (10), 1326–1334.
Chang, Y.H., Lin, C.T., Chen, T.Y., Hsu, C.L., Lee, Y.H., Zhang, W., Wei, K.H., Li, L.J., 2013. Adv. Mater. 25 (5), 756–760.
Dubouis, N., Yang, C., Beer, R., Ries, L., Voiry, D., Grimaud, A., 2018. ACS Catal. 8 (2), 828–836.
Feng, J., Li, F., Li, X., Wang, Y., Fan, D., Du, B., Li, Y., Wei, Q., 2018. Biosens. Bioelectron. 117, 773–780.
Feng, J., Li, Y., Gao, Z., Lv, H., Zhang, X., Fan, D., Wei, Q., 2017. Biosens. Bioelectron. 99, 14–20.
Gao, Z., Li, Y., Zhang, X., Feng, J., Kong, L., Wang, P., Chen, Z., Dong, Y., Wei, Q., 2018. Biosens. Bioelectron. 102, 189–195.
Gupta, A., Arunachalam, V., Vasudevan, S., 2015. J. Phys. Chem. Lett. 6 (4), 739–744.
Heyduk, E., Moxley, M.M., Salvatori, A., Corbett, J.A., Heyduk, T., 2010. Diabetes 59 (10), 2360–2365.
Han, J., Jiang, L., Li, F., Wang, P., Liu, Q., Dong, Y., Li, Y., Wei, Q., 2016. Biosens. Bioelectron. 77, 1104–1111.
Hinnemann, B., Moses, P.G., Bonde, J., Joergensen, K.P., Nielsen, J.H., Horch, S., Chorkendorff, I., Noerskov, J.K., 2005. J. Am. Chem. Soc. 127 (15), 5308–5309.
Hsieh, C.S., Zheng, Y., Liang, Y., Fontenot, J.D., Rudensky, A.Y., 2006. Nat. Immunol. 7 (4), 401–410.
Jasuja, R., Passam, F.H., Kennedy, D.R., Kim, S.H., Hessem, Lv, Lin, L., Bowley, S.R., Joshi, S.S., Dilks, J.R., Furie, B., 2012. J. Clin. Investig. 122 (6), 2104–2113.
Jiang, L., Jian, H., Li, F., Jian, G., Li, Y., Dong, Y., Qin, W., 2015. Electrochim. Acta 160, 7–14.
Karunadasa, H.I., Montalvo, E., Sun, Y., Majda, M., Long, J.R., Chang, C.J., 2012. Science 335 (6069), 698–702.
Laursen, A.B., Vesborg, P.C., Chorkendorff, I., 2013. Chem. Commun. 49 (43), 4965–4967.
Li, F., Han, J., Jiang, L., Wang, Y., Li, Y., Dong, Y., Wei, Q., 2015. Biosens. Bioelectron. 68, 626–632.
Li, F., Li, Y., Feng, J., Gao, Z., Lv, H., Ren, X., Wei, Q., 2018a. Biosens. Bioelectron. 100, 512–518.
Li, M., Wang, P., Pei, F., Yu, H., Dong, Y., Li, Y., Liu, Q., Chen, P., 2018b. Sens. Actuators B: Chem. 261, 22–30.
Liu, Y., Wang, H., Xiong, C., Yuan, Y., Chai, Y., Yuan, R., 2016. Biosens. Bioelectron. 81, 334–340.
Maitra, U., Gupta, U., De, M., Datta, R., Govindaraj, A., Rao, C.N., 2013. Angew. Chem. 52 (49), 13057–13061.
Mercolini, L., Musenga, A., Saladini, B., Bigucci, F., Luppi, B., Zecchi, V., Raggi, M.A., 2008. J. Pharm. Biomed. Anal. 48 (5), 1303–1309.
Merki, D., Fierro, S., Vrubel, H., Hu, X., 2011. Chem. Sci. 2 (7), 1262–1267.
Pandit, S., Karunakaran, S., Boda, S.K., Basu, B., De, M., 2016. ACS Appl. Mater. Interfaces 8 (46), 31567–31573.
Radisavljevic, B., Kis, A., 2013. Nat. Mater. 12 (9), 815–820.
Rather, J.A., De Wael, K., 2012. Sens. Actuators B: Chem. 171–172, 907–915.
Salimi, A., Mohamadi, L., Hallaj, R., Soltanian, S., 2009. Electrochem. Commun. 11 (6), 1116–1119.
Saltiel, A.R., Kahn, C.R., 2001. Nature 414 (6865), 799–806.
Schutte, E., Lambers Heerspink, H.J., Lutgers, H.L., Bakker, S.J., Vart, P., Wolffenbuttel, B.H., Umanath, K., Lewis, J.B., de Zeeuw, D., Gansevoort, R.T., 2015. Am. J. Kidney Dis. Official J. Nat. Kidney Found. 66. pp. 450–458.
Serra-Maia, R., Bellier, M., Chastka, S., Tranhuu, K., Subowo, A., Rimstidt, J.D., Usov, P.M., Morris, A.J., Michel, F.M., 2018. ACS Appl. Mater. Interfaces 10 (25), 21224–21234.
Shi, L., Li, X., Zhu, W., Wang, Y., Du, B., Cao, W., Wei, Q., Pang, X., 2017. ACS Sens. 2 (12), 1774–1778.
Tan, S.M., Ambrosi, A., Sofer, Z., Huber, Š., Sedmidubský, D., Pumera, M., 2015. Chemistry 21 (19), 7170–7178.
Ting, L.R.L., Deng, Y., Ma, L., Zhang, Y.-J., Peterson, A.A., Yeo, B.S., 2016. ACS Catal. 6 (2), 861–867.
Wang, H., Li, H., Zhang, Y., Wei, Q., Ma, H., Wu, D., Li, Y., Zhang, Y., Du, B., 2014. Biosens. Bioelectron. 53, 305–309.
Wang, T., Zhu, H., Zhuo, J., Zhu, Z., Papakonstantinou, P., Lubarsky, G., Lin, J., Li, M., 2013. Anal. Chem. 85 (21), 10289–10295.
Wang, X., Gao, P., Yan, T., Li, R., Xu, R., Zhang, Y., Du, B., Wei, Q., 2018. Sens. Actuators B: Chem. 258, 1–9.
Wu, X., Jin, H., Liu, Z., Ohsuna, T., Terasaki, O., Sakamoto, K., Che, S., 2006. Chem. Mater. 18 (2), 241–243.
Xie, J., Zhang, H., Li, S., Wang, R., Sun, X., Zhou, M., Zhou, J., Lou, X.W., Xie, Y., 2013. Adv. Mater. 25 (40), 5807–5813.
Xu, S., Li, D., Wu, P., 2015. Adv. Funct. Mater. 25 (7), 1127–1136.
Yi, H., Xie, S., Xia, Y., Yuan, R., Chai, Y., 2015. ACS Appl. Mater. Interfaces 7 (24), 13360–13366.
Zhang, S., Chowdari, B.V.R., Wen, Z., Jin, J., Yang, J., 2015. ACS Nano 9 (12), 12464–12472.
Zhu, W., Wang, C., Li, X., Khan, M.S., Sun, X., Ma, H., Fan, D., Wei, Q., 2017. Biosens. Bioelectron. 97, 115–121.